Vapor chemical composition in Electron Beam Powder Bed Fusion using Ti-6Al-4V powder

Vinicius Antunes, Abderzak El Farsy, Angela Crespi, Charles Ballage, Ovidiu Vasilovici, Patrick Chapon, Camille Petit-Etienne, Erwine Pargon, Tiberiu Minea

Vapor chemical composition in Electron Beam Powder Bed Fusion using Ti-6Al-4V powder

Vinicius G. Antunes[1,2*], Abderzak El Farsy[1], Angela Crespi[1], Charles Ballage[1], Ovidiu Vasilovici[1], Patrick Chapon[3], Camille Petit-Etienne[2], Erwine Pargon[2], Tiberiu Minea[1]

[1]*Université Paris-Saclay, CNRS, Laboratoire de physique des gaz et des plasmas, 91405, Orsay, France.*

[2]*Univ. Grenoble Alpes, CNRS, CEA/LETI-Minatec, Grenoble INP, LTM, Grenoble F-38054, France*

[3]*HORIBA France, Bd Thomas Gobert, 91120 Palaiseau, France*

Abstract

This study investigates the vapor chemical composition, during the melting step of an Electron Beam Powder Bed Fusion process using Ti-6Al-4V powder. A phenomenological model is proposed to analyze and discuss the vapor composition. The model focus on the heat dissipation of the molten powder. Vapor stream from the molten powder is compounded by vapor saturation pressure and rapid boiling (ebullition) of the molten pool. The model is based on *post mortem* results of condensed vapor (thin film), which were analyzed by X-ray Photoelectron Spectroscopy and Glow Discharge Optical Emission Spectrometry, providing quantitative and in-depth profile data. It was found that the ratio of [Al] to [Ti] in the vapor stream is influenced by the melting conditions. As the e-beam current increases, the heat dissipation reaches the ebullition domains, and the [Al]/[Ti] ratio tends to the molar ratio of the precursor powder (Ti-6Al-4V), indicating the complete overheating of all the alloy elements.

Keywords: E-PBF; Vapor; Chemical Composition; Evaporation Model; Thin Film; Thermal Regimes

*Correspondent author: vinicius.antunes@cea.fr

1. Introduction

Additive manufacturing has revolutionized the way parts are designed and produced, offering innovative solutions and unique designs [1–3]. Among various additive manufacturing processes, Electron Beam Powder Bed Fusion (E-PBF) is widely favored for its speed and its ability to minimize residual stress in printed parts [3]. E-PBF involves a four-step process: lowering the build plate, spreading the powder to form a bed, pre-heating the powder (pre-sintering), and selectively melting the powder at specific locations according to the design. Fig. 1 illustrates the schematic of the E-PBF process. The precise adjustment of the parameters during the melting step directly influences the part's mechanical properties and the quality of the microstructure between consecutive layers. However, inadequate power delivery can result in porosity and voids in the final part.

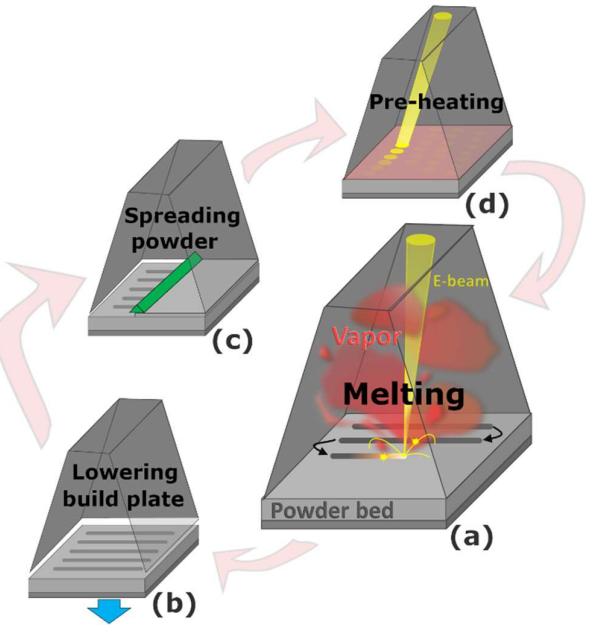

Figure 1. A schematic diagram of the four-step process in E-PBF, illustrating (a) melting the powder, (b) lowering the build plate, (c) spreading the powder to form a bed, and (d) pre-heating the powder.

Regarding the melting process, the volumetric energy density (*VED*) and hatching strategy play a crucial role in determining the characteristics of the heat-affected zone, molten pool, and depression zone [3–11]. The $VED \propto \frac{P}{v}$, where P is the beam power and v the scan speed [5].

Properly tuning the *VED* determines whether the thermal regime is conduction or the keyhole regime, which greatly impacts the success of the melting process [5]. The shape of the molten pool, which is crossed along the e-beam scan axis, depends on how heat is dissipated [5]. Figure 2Fig. 2 depicts the schematic shape of the molten pool. In the conduction regime, the heat dissipation results in a shallow depression zone and well-distributed VED in the heat-affected zone [12]. This leads to selective evaporation of volatile elements in the powder alloy, resulting in less content of these elements in the built part [13–16]. The vapor pressure is the evaporation stream produced by a hot surface below its boiling point [17]. In the keyhole regime, the molten pool has a chalice shape, and the depression zone takes on a needle-like shape filled with vapor [12, 18]. The ebullition of the molten pool in the depression zone preserves the alloy stoichiometry in the vapor chemical composition.

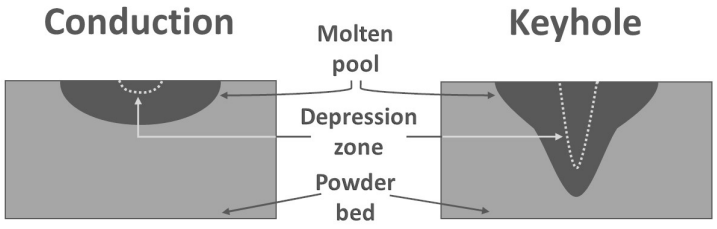

Figure 2. A schematic representation of the shapes of the molten pool and depression zone as a function of the assessed thermal regime, typically distinguishing between the heat conduction and keyhole.

The depression zone, where the e-beam interacts with the molten pool, shows the spatial inhomogeneity of vapor production in the heat-affected zone. The recoil pressure of the vapor affects the shape of depression zone [14, 16, 19]. Notably, ebullition creates a vapor stream (vapor plume), which combines with the vapor pressure from the molten pool to form the total vapor [17]. The contribution of ebullition and vapor pressure to the total vapor varies with VED and the hatching strategy. Therefore, the chemical composition of the vapor is closely related to how the heat was dissipated in the alloy powder. It is important to note that the operating pressure during this study was maintained at 0.2 Pa of helium, enabling the released vapor to travel with minimal dispersion from depression zone to the heat shield walls.

The vapor released from heated Ti-6Al-4V alloy has garnered interest from numerous researches groups [20–30]. This interest arises primarily because printed parts tend to lack Al [20, 21, 23, 28], which is attributed to the lower melting point of Al compared to the other alloy elements [20, 22, 29]. Consequently, the process understanding requires addressing both

external operation parameters and the chemical composition of the vapor. Advancements in this understanding comprehension are crucial for developing technological innovations that enhance the quality of printed parts and the overall reliability of the process.

To enhance real-time monitoring, researchers have investigated the chemical composition of the vapor released during parts manufacturing in an industrial E-PBF machine [22, 31–33]. The principle is that changes in the powder melting affect the chemical composition and rate of vapor production. When the formed vapor reaches the inner walls of the experimental chamber, it forms a thin film, which serves as a thermal memory of the powder's melting process. Therefore, the focus of the study is on the *post mortem* chemical analysis of the condensed vapor. The objective is to propose a model for the vapor's chemical composition and support it with experimental analyses, while establishing its relationship with the thermal melting regime of the powder. The model has the potential to monitor the melting process, enabling real-time adjustment of external process parameters among consecutive layers or revealing the thermal history of the melting process through *post-mortem* analysis of the condensed vapor.

2. Experimental Details

The ARCAM A1 machine (GE Additive) was operated under two conditions labeled 'constant' (non-optimized) and 'optimized'. In the 'optimized' condition, the ARCAM A1 software controlled the scan speed, hatching, and e-beam current. In the non-optimized procedure, the beam current, hatching strategy (snake-like hatching without contour), and scan speed were fixed, see Table 1. The e-beam profile of the optimized and non-optimized are display in Fig. 3. All samples were produced using the same operation conditions: an acceleration voltage of 60 kV, a spot size of approximately 250 μm diameter, and a powder layer thickness of 50 μm. No supports were used, and the parts were built directly on the stainless-steel build plate.

Fig. 3 (a) depicts the different e-beam current sequences, including pre-heat and melt phases. During the pre-heat phase, a high current of 35 to 40 mA and a defocused e-beam were used to pre-sinter the powder, maintaining the powder temperature at 850°C. The melting phase utilized a focused e-beam with a higher current density. Fig. 3 (b) compares the melting e-beam

profiles, showing variations in e-beam current among different samples. The nominal average current for the optimized sample was 8.7 mA (O8), while constant e-beam current samples had values of 2, 3, and 5 mA, respectively labeled as C2, C3, and C5.

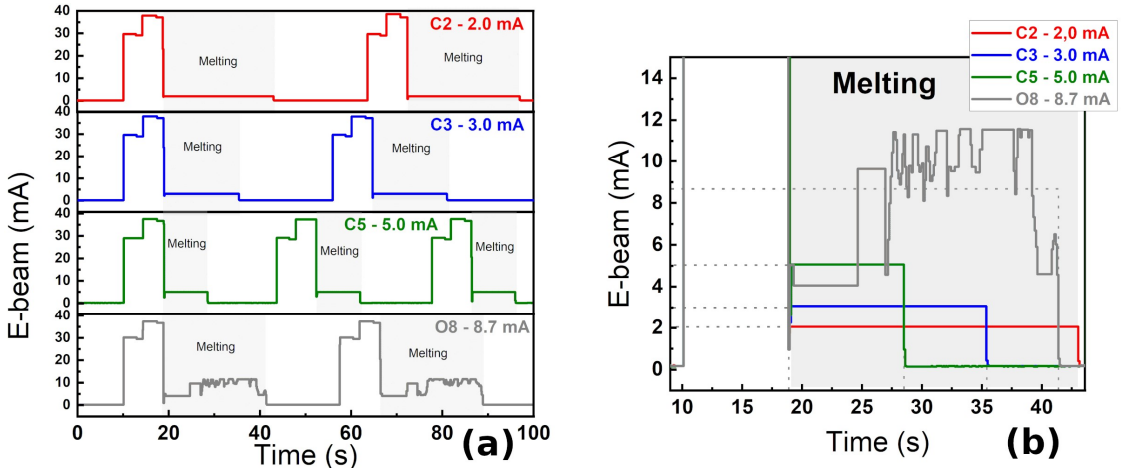

Fig. 3 (a)E-beam current sequences versus time during the part building. (b) E-beam profile during the melting stage for different e-beam currents

Table 1 summarizes the data of Fig. 3, displaying the nominal e-beam current, beam power, and scan speed. The Ti-6Al-4V alloy powder used had a statistical diameter distribution ranging from 45 to 106 µm (Arcam Titanium Ti6Al4V ELI, GE). For each experiment, four cubes with 15 mm edges were printed, each centered 7 cm away from the build plate corners along the diagonal. The chamber base pressure was 10^{-3} Pa, and the working pressure was 0.2 Pa of He.

Table 1. Sample's identification, e-beam current, e-beam power, and VED. The C2, C3, and C5 denote constant e-beam currents at 2, 3, and 5 mA, respectively. O8 denotes the optimized (Arcam) melting sequence with a nominate e-beam current of 8.7 mA

Sample	Parameters Optimization	Primary E-beam (mA)	E-beam Power (W)	Scan Speed (m/s)
C2	No	2	100	0,12
C3	No	3	150	0.22

C5	No	5	300	0.35
O8	Yes	8.7	522	0.15

Thin films were grown on a substrate placed 40 cm above the powder bed, on the top of the heat shield, Fig. 4 (a). Two substrates were used: copper foil (50 μm thick and 99.999% of purity) and Si (mono-crystalline, <100>, B doped with 1 - 5 Ωcm of resistivity), attempting to investigate if the substrate could influence the chemical composition of the condensed vapor. Nevertheless, no differences were observed between the samples on the two substrates used in the study. The chemical composition of the thin films was analyzed in-depth using Glow Discharge Optical Emission Spectrometry, GDOES (GD-Profiler 2^{TM}, HORIBA), and the quantitative analysis of the surface by X-Ray Photoelectron Spectroscopy, XPS (Theta 300, ThermoFisher). The deposition rate was measured using Quartz Crystal Micro Balance (STM-2, INFICON). The thickness of the thin film was measured using a 3D optical profilometer (ContourX-200, Bruker).

3. Phenomenological model for the vapor origin in E-PBF

The present model draws inspiration from studies on e-beam evaporation [17, 28, 34], e-beam welding [18, 35], Laser Powder Bed Fusion (L-PBF) [5, 8, 9, 20, 29, 36, 37], E-PBF [14, 19, 21, 38, 39] and Ti-6Al-4V material [9, 20, 21, 23–25, 28, 29].

Two physical phenomena contribute to the production of metal vapors in E-PBF process: molten pool evaporation, also known as vapor pressure (liquid – A, Fig. 4 (b)) together with race track evaporation (solid – A', Fig. 4 (b)), as well as ebullition in the depression zone (B, Fig. 4 (b)). Indeed, the second phenomenon takes place once the boiling temperature of the molten pool is locally reached, or passed in the overheated cases.

The characteristics of the vapor streams, such as evaporation rates and chemical composition, are determined by their respective sources (Fig. 4 (b)). The molten pool has two solid-liquid interfaces, one in contact with the solidified trace behind the energetic beam and the other touching the powder, mostly a head of the energetic beam (Limit I – Fig. 4 (b)). These

interfaces are defined by the melting point (in case of Ti ~1923 K at atmospheric pressure) [9, 40]. The depression zone is defined by the liquid-gas interface and is formed and maintained over a complex group of forces through interactions between the gas and liquid phases [35] (Limit II – Fig. 4 b). The boiling temperature of the Ti-6Al-4V alloy is at 3133 K at atmospheric pressure and 1949 K at 0.2 Pa [20, 29]. Works have shown that the molten pool overheated in vicinity of depression zone, reaching 3300 K [41, 42]. The exposed surface of the molten pool to the chamber has a temperature gradient from the race track towards depression zone. The vapor stream is influenced by the local temperature, with the maximum concentration occurring at the depression zone[37].

The stream of the vapor pressure from the race track (process A', hot solid metal) is negligible compared to the vapor pressure from the molten pool (process A) and ebullition in the depression zone (process B). Thus, we have discarded the vapor pressure contribution from race track from the model.

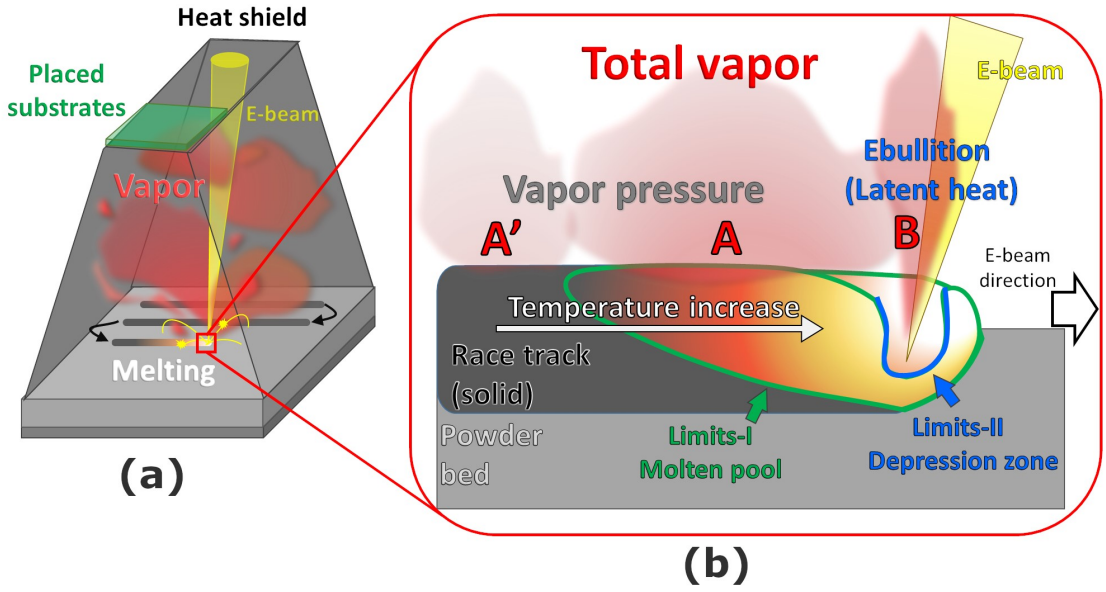

Fig. 4 a) Sketch illustrating of the E-PBF melting process. Topmost square region (green) indicates where the deposited vapor was collected. b) Vapor pressure (equilibrium) at interfaces: A' - solid race track / gas; A - molten pool/gas, and B - ebullition liquid/gas (latent heat). The limit-I of the solid-liquid plus liquid-gas determines molten pool and limit-II liquid-gas at depression zone

The vapor pressure of a pure material can be described by Clausius-Clapyeron equation, $p = p_0 e^{-\frac{\Delta H_e}{RT}}$, which assumes a constant the evaporation enthalpy (ΔH_e) [43], perfect gas constant (R), temperature (T) and pre-factor (p_0) [17]. Adding corrections for molar fraction

(X) and activity coefficient (γ) [20], the equation can be written as $p_i = \gamma_i X_i p_{0_i} e^{-\frac{\Delta H_e^i}{RT}}$ (Raoult's law) where i is an element composing the alloy [17]. Each alloy element will have a specific vapor pressure, with the vapor pressure of Ti-6Al-4V being $p_{Al} \gg p_{Ti} > p_V$. The high cooling rates of E-PBF (10^3 to 10^5 K/s [1]) discard the effect of changing alloy molar fraction during the melting stage. Moreover, the vapor stream from ebullition preserves the molar ratio of the alloy composing the powder in the vapor phase.

Fig. 5 represents the partial pressure ratio of Al and Ti $\left(\frac{p_{Al}}{p_{Ti}}\right)$ as a function of melted Ti-6Al-4V, showing the transition and changes in element predominance in the vapor phase along the molten pool. The temperature gradient depict in the figure extends from 1920 K to 1960 K [20]. The vapor pressure ratio calculate by Raoult's law is represented in-dash gray, and, in-dash light blue, the molar fraction of Al with respect to Ti in Ti-6Al-4V powder (~0.067). The transition between two curves is not analytical, it was supposed to be continue and center at the boiling point at 0.2 Pa. The depth of the molten pool, d, should be at least two times the bed layer thickness, λ, in order to build a part.

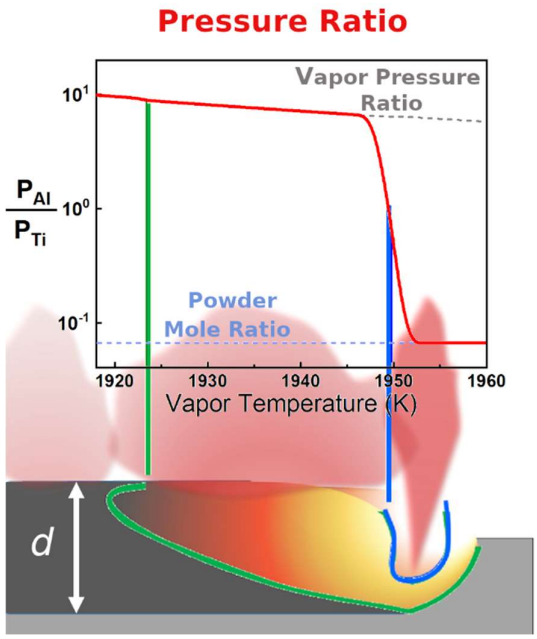

Fig. 5 The phenomenological model for the vapor composition along the molten pool. The graph represents the relative partial pressure of Al to Ti versus temperature. The melting (green) and boiling (blue) points are highlighted

Consequently, the total vapor results from the sum of molten pool evaporation (vapor pressure) and depression zone (ebullition). When considering the ratio of partial pressure in the total vapor, if $\left(\frac{p_{Al}}{p_{Ti}}\right) > 1$, indicating that the vapor is rich in Al, the vapor pressure plays a significant role. In this scenario, the conduction thermal regime dominates the heat dissipation in the molten pool. Conversely, if $\left(\frac{p_{Al}}{p_{Ti}}\right) < 1$, it signifies that ebullition has a major impact on total vapor production, which is induced by the keyhole thermal regime.

4. Chemical composition of condensed vapor

The vapor in the E-PBF machine reaches the inner walls of the heat shield and main chamber, where it condenses and forms a thin film. The atoms in the vapor may undergo thermalization along their path, resulting in their energy being close to the temperature of the main chamber. However, in the vicinity of the depression zone, the vapor temperature can reach up to 6000 K [37]. Empirically, it has been observed that the top of the heat shield reaches a temperature of approximately 400 K after nearly 7h of printing. Therefore, we can disregard the desorption of the condensed vapor and any chemical selectivity along the path of the vapor. Furthermore, it is only during the melting step that the vapor produces a thin film. During the pre-heat phase, the vapor stream maintains a very low rate, thus not significantly contributing to the growth of the thin film.

The chemical composition of the samples, as determined by XPS, is presented in Table 2. It provides the relative atomic concentration of titanium (Ti), aluminum (Al), vanadium (V), and contaminants such as carbon (C), oxygen (O), silicon (Si), and copper (Cu). These atomic concentrations correspond to the elements present on the surface of the sample. Despite the contamination and the effects of packing and transportation, what should be likely the cause of such a high [O] and [C], the concentration ratio of Al and Ti ($\frac{[Al]}{[Ti]}$) remains unchanged. Fig. 6 illustrates the concentration ratio of the components of the thin films $\frac{[Al]}{[Ti]}$ as a function of the e-beam current. The deposition rate of the thin films is also reported as well in the last column of Table 2.

Table 2. Relative Atomic Concentration and deposition rate of the thin films grown during the part build with the e-beam current presented in Fig. 3

Samples	Relative Atomic Concentration (%)							Deposition rate (Å/s) ± 0.1
	[Ti]	[Al]	[V]	[C]	[O]	[Si]	[Cu]	
C2	3.0	6.9	<0.1	40.4	39.3	10.4	--	<0.2
C3	5.4	7.8	<0.1	47.6	38.9	--	0.3	0.2
C5	2.4	2.5	<0.1	40.7	38.9	15.5	--	0.7
O8	4.3	5.0	<0.1	42.8	40.0	7.9	--	1.9

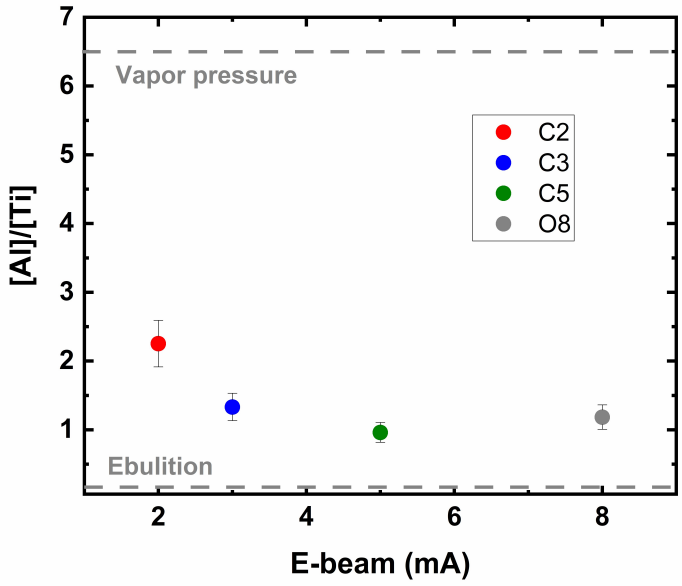

Fig. 6 Ratio of [Al] and [Ti] as a function of the e-beam current. The dashed lines depict the expected [Al] over [Ti] ratio if due to pure vapor pressure (top) or pure ebullition (bottom)

Fig. 6 highlights two domains: vapor pressure and ebullition. The dashed bottom line represents the powder molar fraction ratio, $\frac{[Al]}{[Ti]} \sim 0.067$, assuming that ebullition does not affect

the alloy composition in the gas phase. The top dashed line at $\frac{[Al]}{[Ti]} \sim 6.5$ corresponds to the ratio of the vapor pressure at the boiling point of Al calculated using Raoult's corrected law.

Regarding the molten pool depth (d), it must be larger, or at least equal, to two powder bed layers (2λ) to join them in building a part. Nevertheless, electron absorption occurs in less than one layer (λ = 50 μm) [44, 45]. Therefore, overheating of the molten pool is necessary to increase d, which leads to an increased contribution of the ebullition in heat dissipation. It worth noting that the Fig. 6 evidence the contribution of the e-beam power and hatching strategy to the ebullition.

Disregarding the O8 sample, as the e-beam current increases, the [Al]/[Ti] ratio shifts drastically, especially when the molten pool temperature approaches the Al ebullition point, indicating a much higher contribution of the depression zone in the total vapor stream. Additionally, the deposition rate also increases with the e-beam current, Table 2. Moreover, the impact of the hatching strategy becomes evident when comparing the optimized process (O8) with non-optimized process at higher e-beam current (C5). Despite O8 having higher average current than C5, its [Al]/[Ti] ratio remains slightly higher than C5, suggesting lesser ebullition contribution in the total vapor. This is due to the hatching strategy's influence on the overheating of the molten pool, signifying that the chemical composition of the condensed vapor retains a memory of the melting conditions.

Fig. 7 highlights the effect of the thermal memory on the vapor deposited as a thin film. The emission intensity ratio $\frac{I_{Al}}{I_{Ti}}$, recorded by Glow Discharge Optical Emission Spectroscopy (GDOES), is shown in-depth profile. The depth was normalized with the thickness of the thin films, with the z–axis ranging from the surface (z = 0) to the interface between the thin film and the substrate (z = 1).

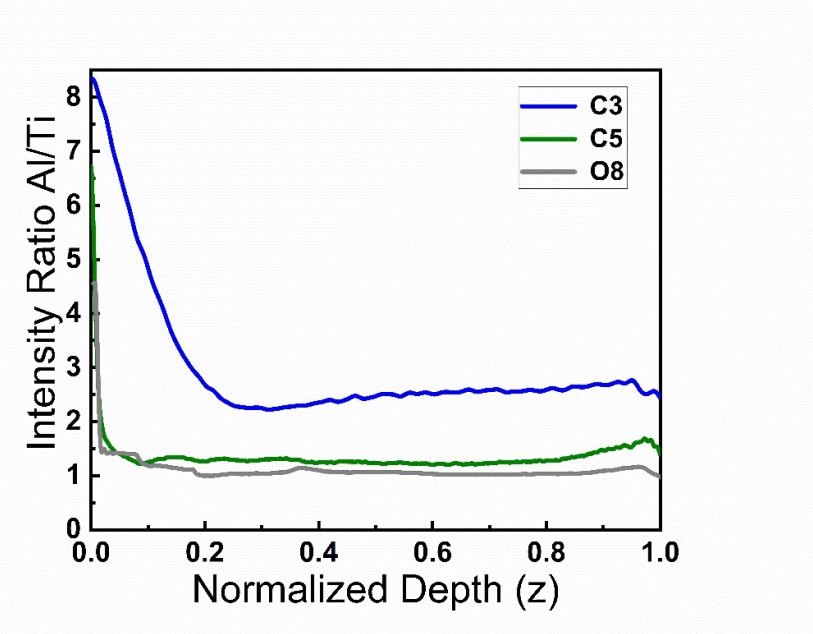

Fig. 7 The GDOES renormalized depth profiles of the emission line intensity ratio of $\frac{I_{Al}}{I_{Ti}}$ for several thin films. Conditions are given in Table 2

The intensity of $\frac{I_{Al}}{I_{Ti}}$ decreases with the e-beam current, and it is higher at the surface of the thin film (z=0) due to the melting of the very last layer of the metallic powder. However, it diminishes at the interface between the thin film and the substrate, indicating a drastic change in the molten bath thermodynamics at the start and end of the printing process.

At the end of the printing process, z = 0, the surface reflects the cooling of the printed part along with the heated affected zone. As Fig. 5 shows, the released vapor from the last (upper) molten layer increases the content of Al in the deposited layer. During the cooling process, the temperature reduction of the free (upper) surface propitiates more Al vapor compared to Ti. Consequently, the film is aluminum rich at extreme surface. In the inner layers, z = 0.2 to z = 0.8, the $\frac{I_{Al}}{I_{Ti}}$ ratio remains constant due to the quasi-stationary total vapor stream composition. Then, the system remained in constant melting conditions, leading to a plateau of the $\frac{I_{Al}}{I_{Ti}}$ ratio. However, at the beginning of the melting (z > 0.8), deviations in the $\frac{I_{Al}}{I_{Ti}}$ trend are observed, potentially due to the properties of a compound formed from the mixture of powder and build plate materials. At that moment, the build plate has been melted together with the powder. After several layers, the thickness of the melted part increases leaving the system to a quasi-stationary generation of total vapor stream.

The diffusion of film constituents, particularly Al, towards the surface is facilitated by the energy brought by the evaporated species, resulting in a higher $\frac{I_{Al}}{I_{Ti}}$ ratio in thinner films, which is the case of condition C3, see Table 2. This inter-element diffusion is also visible on the iron (Fe), recorded as traces in the deposited film (Fig. 8).

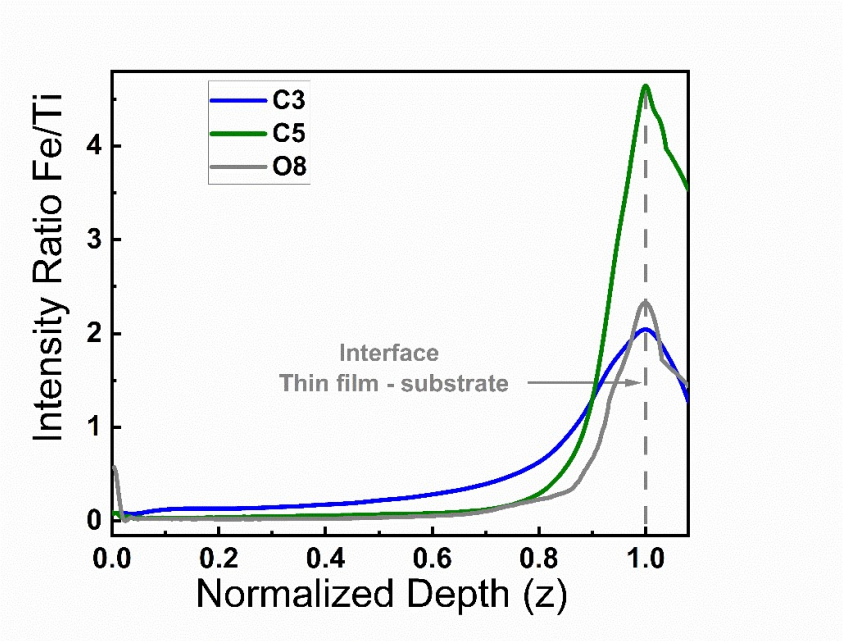

Fig. 8 The GDOES depth profiles of the intensity ratio I_{Fe}/I_{Ti} for thin film obtained in different conditions reported in Table 2

Fig. 8 shows the Fe signature across the film's thickness. As expected, the Fe dominates near the thin film-substrate interface. This suggest that Fe was evaporated at the beginning of the printing process when the first layers were melted. The presence of Fe can be easily explained since the build plate is made of stainless steel and the melting penetration depth, *d,* is higher than one powder bed thickness (λ).

As demonstrate above, the chemical composition of the vapor carries a signature of the melting process, which is particularly useful for understanding the depression zone and keyholing. Therefore, the chemical composition of the vapor can be utilized for real-time monitoring of the melting process using techniques such as mass spectrometry or light absorption [22]. This allows the controller to adjust the e-beam parameters in real-time. Another

possibility is to conduct a *post-mortem* analysis, as discussed in this study, where the thermal history of the melting process is preserved as a thin film.

5. Conclusions

A phenomenological model, derived from the analysis of systematic experiments on the vapor chemical composition in the E-PBF process, has been proposed in this study. The model suggest that the appearance of the vapor stream is influenced by the vapor pressure and ebullition. The vapor pressure is present in the race track and molten pool, while ebullition occurs in the depression zone. The size and characteristics of these regions are directly dependent on the melting parameters, particularly the beam power. Therefore, the vapor released from these heated regions retains information about the melting process, resulting in a unique chemical composition in the condensed vapor.

The concentration ratio of [Al] to [Ti] in the vapor is found to be highly sensitive to the e-beam current. This ratio can be used to qualitatively compare the contribution of the ebullition and vapor pressure in the thin films, allowing for an evaluation of the balance between the volume of the depression zone and the liquid metal area. Additionally, the chemical composition of the collected thin film can help identify the thermal regimes achieved during the process, such as conduction and keyhole, as well as the thermal history of the molten layers.

6. Reference

1. Liu S, Shin YC (2019) Additive manufacturing of Ti6Al4V alloy: A review. Mater Des 164:107552. https://doi.org/10.1016/j.matdes.2018.107552
2. Li N, Huang S, Zhang G, et al (2019) Progress in additive manufacturing on new materials: A review. J Mater Sci Technol 35:242–269. https://doi.org/10.1016/j.jmst.2018.09.002
3. Körner C (2016) Additive manufacturing of metallic components by selective electron beam melting - A review. Int Mater Rev 61:361–377. https://doi.org/10.1080/09506608.2016.1176289
4. Galati M, Iuliano L, Salmi A, Atzeni E (2017) Modelling energy source and powder properties for the development of a thermal FE model of the EBM additive

manufacturing process. Addit Manuf 14:49–59. https://doi.org/10.1016/j.addma.2017.01.001

5. Guo Q, Zhao C, Qu M, et al (2019) In-situ characterization and quantification of melt pool variation under constant input energy density in laser powder bed fusion additive manufacturing process. Addit Manuf 28:600–609. https://doi.org/10.1016/j.addma.2019.04.021

6. Ledford C, Tung M, Rock C, Horn T (2020) Real time monitoring of electron emissions during electron beam powder bed fusion for arbitrary geometries and toolpaths. Addit Manuf 34:101365. https://doi.org/10.1016/j.addma.2020.101365

7. Singh N, Hameed P, Ummethala R, et al (2020) Selective laser manufacturing of Ti-based alloys and composites: impact of process parameters, application trends, and future prospects. Mater Today Adv 8:100097. https://doi.org/10.1016/j.mtadv.2020.100097

8. Guo Q, Zhao C, Qu M, et al (2020) In-situ full-field mapping of melt flow dynamics in laser metal additive manufacturing. Addit Manuf 31:100939. https://doi.org/10.1016/j.addma.2019.100939

9. Zhao C, Fezzaa K, Cunningham RW, et al (2017) Real-time monitoring of laser powder bed fusion process using high-speed X-ray imaging and diffraction. Sci Rep 7:1–11. https://doi.org/10.1038/s41598-017-03761-2

10. Gong X, Anderson T, Chou K (2014) Review on powder-based electron beam additive manufacturing Technology. Manuf Rev 1:. https://doi.org/10.1051/mfreview/2014001

11. Raplee J, Plotkowski A, Kirka MM, et al (2017) Thermographic Microstructure Monitoring in Electron Beam Additive Manufacturing. Sci Rep 7:1–16. https://doi.org/10.1038/srep43554

12. DePond PJ, Fuller JC, Khairallah SA, et al (2020) Laser-metal interaction dynamics during additive manufacturing resolved by detection of thermally-induced electron emission. Commun Mater 1:1–10. https://doi.org/10.1038/s43246-020-00094-y

13. Zhou J, Li H, Yu Y, et al (2019) Intermetallics Research on aluminum component change and phase transformation of TiAl-based alloy in electron beam selective melting process under multiple scan. Intermetallics 113:106575. https://doi.org/10.1016/j.intermet.2019.106575

14. Klassen A, Forster VE, Juechter V, Körner C (2017) Numerical simulation of multi-component evaporation during selective electron beam melting of TiAl. J Mater Process Tech 247:280–288. https://doi.org/10.1016/j.jmatprotec.2017.04.016

15. Popov V V, Katz-demyanetz A, Koptyug A (2019) Selective electron beam melting entropy alloys using elemental powder blend. Heliyon e01188. https://doi.org/10.1016/j.heliyon.2019.e01188

16. Panwisawas C, Gong Y, Tony Y, et al (2021) Additive manufacturability of superalloys : Process-induced porosity , cooling rate and metal vapour. Addit Manuf 47:102339. https://doi.org/10.1016/j.addma.2021.102339

17. Ohring M (2002) Thin-Film Evaporation Processes. Mater Sci Thin Film 95–144. https://doi.org/10.1016/b978-012524975-1/50006-9

18. Singh R (2020) Physics of welding

19. Fu Z, Körner C (2022) Actual state-of-the-art of electron beam powder bed fusion. Eur J Mater 2:54–117. https://doi.org/10.1080/26889277.2022.2040342

20. Zhang G, Chen J, Zheng M, et al (2020) Element vaporization of Ti-6AL-4V alloy during selective laser melting. Metals (Basel) 10:1–14. https://doi.org/10.3390/met10040435

21. Juechter V, Scharowsky T, Singer RF, Körner C (2014) Processing window and evaporation phenomena for Ti-6Al-4V produced by selective electron beam melting. Acta Mater 76:252–258. https://doi.org/10.1016/j.actamat.2014.05.037

22. Farsy A El, Antunes VG, Seznec B, et al (2022) Saturation pressure of nonequilibrium titanium evaporation during additive manufacturing by electron powder bed fusion. J Appl Phys 132:. https://doi.org/10.1063/5.0091349

23. Wang D, Liu Z, Liu W (2021) Experimental measurement of vacuum evaporation of aluminum in ti-al, v-al, ti6al4v alloys by electron beam. Metals (Basel) 11:. https://doi.org/10.3390/met11111688

24. Mishra AK, Kumar A, Govind (2023) Development and validation of a material evaporation assisted thermal model for time-efficient calculation of thermal and solidification parameters during laser powder bed fusion process for Ti6Al4V. Addit Manuf 66:103453. https://doi.org/10.1016/j.addma.2023.103453

25. Guo Q, Zhao C, Escano LI, et al (2018) Transient dynamics of powder spattering in laser powder bed fusion additive manufacturing process revealed by in-situ high-speed high-energy x-ray imaging. Acta Mater 151:169–180. https://doi.org/10.1016/j.actamat.2018.03.036

26. Mishra AK, Kumar A (2024) Development and application of a simplified thermo-evaporative multi-track laser powder bed fusion model for Ti6Al4V. Int J Therm Sci 197:108816. https://doi.org/10.1016/j.ijthermalsci.2023.108816

27. Bartsch K, Herzog D, Bossen B, Emmelmann C (2021) Material modeling of Ti–6Al–4V alloy processed by laser powder bed fusion for application in macro-scale process simulation. Mater Sci Eng A 814:141237. https://doi.org/10.1016/j.msea.2021.141237

28. Westerberg KW, Meier TC, Mcclelland MA, et al (1997) Analysis of the E-Beam Evaporation Titanium and Ti-6Al-4V. In: Electron Beam Melting and Refining State of the Art 1997 Conference. Reno, Nevada

29. Zhou B, Zhou J, Li H, Lin F (2018) A study of the microstructures and mechanical properties of Ti6Al4V fabricated by SLM under vacuum. Mater Sci Eng A 724:1–10. https://doi.org/10.1016/j.msea.2018.03.021

30. Klassen A, Forster VE, Körner C (2017) A multi-component evaporation model for beam melting processes. Model Simul Mater Sci Eng 25:. https://doi.org/10.1088/1361-651X/aa5289

31. Everton SK, Hirsch M, Stavroulakis PI, et al (2016) Review of in-situ process monitoring and in-situ metrology for metal additive manufacturing. Mater Des 95:431–445. https://doi.org/10.1016/j.matdes.2016.01.099

32. Boone N, Zhu C, Smith C, et al (2018) Thermal near infrared monitoring system for

electron beam melting with emissivity tracking. Addit Manuf 22:601–605. https://doi.org/10.1016/j.addma.2018.06.004

33. Cordero PM, Mireles J, Ridwan S, Wicker RB (2017) Evaluation of monitoring methods for electron beam melting powder bed fusion additive manufacturing technology. Prog Addit Manuf 2:1–10. https://doi.org/10.1007/s40964-016-0015-6

34. Bishop CA (2015) Electron Beam (e-Beam) Evaporation. In: Vacuum Deposition Onto Webs, Films and Foils, 3rd ed. Elsevier, pp 289–299

35. Węglowski MS, Błacha S, Phillips A (2016) Electron beam welding - Techniques and trends - Review. Vacuum 130:72–92. https://doi.org/10.1016/j.vacuum.2016.05.004

36. Leung CLA, Marussi S, Atwood RC, et al (2018) In situ X-ray imaging of defect and molten pool dynamics in laser additive manufacturing. Nat Commun 9:1–9. https://doi.org/10.1038/s41467-018-03734-7

37. Bidare P, Bitharas I, Ward RM, et al (2018) Fluid and particle dynamics in laser powder bed fusion. Acta Mater 142:107–120. https://doi.org/10.1016/j.actamat.2017.09.051

38. Antunes VG, Farsy A El, Seznec B, Minea T (2024) Thermionic electrons in electron beam powder bed fusion process : An experimental investigation. Addit Manuf 80:103957. https://doi.org/10.1016/j.addma.2024.103957

39. el Farsy A, Tighidet EC, Ballage C, Minea T (2023) Spatiotemporal characterization of evaporated atoms during electron beam melting additive manufacturing by advanced laser diagnostics. J Appl Phys 133:044901. https://doi.org/10.1063/5.0131102

40. Song J, Wang L, Zhang L, et al (2020) First-principles molecular dynamics studying the solidification of Ti-6Al-4 V alloy. J Mol Liq 315:113606. https://doi.org/10.1016/j.molliq.2020.113606

41. Klassen A, Scharowsky T, Körner C (2014) Evaporation model for beam based additive manufacturing using free surface lattice Boltzmann methods. J Phys D Appl Phys 47:. https://doi.org/10.1088/0022-3727/47/27/275303

42. Cook PS, Murphy AB (2020) Simulation of melt pool behaviour during additive manufacturing: Underlying physics and progress. Addit Manuf 31:100909. https://doi.org/10.1016/j.addma.2019.100909

43. Chase M (1998) NIST-JANAF Thermochemical Tables, fourth. U.S. Secretary of Commerce on behalf of the United States, New York

44. Zäh MF, Lutzmann S (2010) Modelling and simulation of electron beam melting. Prod Eng 4:15–23. https://doi.org/10.1007/s11740-009-0197-6

45. Gong X, Cheng B, Price S, Chou K (2013) Powder-bed electron-beam-melting additive manufacturing: powder characterization, process simulation and metrology. Early Career Tech Conf Birmingham, AL 55–66

Funding

This study was performed in the framework of the SOFIA project supported by BPI France. We thank also the french RENATECH network.

Conflicts of interest

The authors declare no competing interests.

Availability of data and material

The data supporting the conclusions are included in the article.

Code availability

Not applicable

Ethics approval

The authors confirm that they have abided by the publication ethics and state that this work is original and has not been used for publication anywhere before.

Consent to participate

The authors are willing to participate in journal promotions and updates.

Consent for publication

The authors grant the publisher the sole and exclusive license of the full copyright in the contribution.

Authors contribution

Vinicius G. Antunes: conceptualization, data curation, methodology, investigation, experiments, writing of original draft, validation, and writing including review and editing; Abderzak El Farsy: experiment, writing including review and editing, and validation; Angela Crespi: writing including review and editing, and validation; Charles Ballage: experiment, writing including review and editing, and validation; Ovidiu Vasilovici: experiment, writing including review and editing, and validation; Patrick Chapon: experiment, writing including review and editing, and validation; Camille Petit-Etienne: experiment, writing including review and editing, and validation; Erwine Pargon: writing including review and editing, validation, and supervision. Tiberiu Minea: project administration, writing including review and editing, conceptualization, and supervision. All authors read and approved the final manuscript.

Acknowledgements

We are indebted to S. Gaiaschi, and J. Marciano from Horiba for the GDOES measurements. The authors are grateful to Rémi Daniaud for the technical help.